

Detection of the prototype symmetry of ferroelastic WO₃ domain walls by angle-resolved polarized Raman spectroscopy

Jeongdae Seo,^{1,2,*} Ho-Hyun Nahm^{1,*}, Heung-Sik Park,^{1,2} Shinhee Yun³, Jin Hong Lee,¹ Yong-Jin Kim^{1,2}, Yong-Hyun Kim^{1,†} and Chan-Ho Yang^{1,2,‡}

¹*Department of Physics, Korea Advanced Institute of Science and Technology, Daejeon 34141, Republic of Korea*

²*Center for Lattice Defectronics, Korea Advanced Institute of Science and Technology, Daejeon 34141, Republic of Korea*

³*Department of Energy Conversion and Storage, Technical University of Denmark, Kongens Lyngby 2800, Denmark*



(Received 7 February 2022; revised 17 June 2023; accepted 26 June 2023; published 10 July 2023)

The symmetry of a domain wall in ferroelastic WO₃ is analyzed by angle-resolved polarized Raman spectroscopy. We find that a low-energy Raman mode at 46 cm⁻¹ is largely enhanced within the confined region of the domain wall, whose width is presumed to be ~25 nm from diffusive x-ray scattering. The wall effect on the enhancement of the Raman signal per unit area is estimated to be three times larger than the contribution of the domains. The light-polarization-dependent Raman intensity at the wall is characterized by the symmetric A_{1g} Raman tensor that is attributed to the prototypic quasitragonal phase imposed by the ferroelastic compatibility relationship.

DOI: [10.1103/PhysRevB.108.014103](https://doi.org/10.1103/PhysRevB.108.014103)

I. INTRODUCTION

Ferroelastic domain walls are of interest because of their association with a variety of interfacial phenomena, including electrical polarization, piezoelectricity, nonlinear optical response, electronic conduction, and superconductivity [1–3]. Boundaries or walls between two different orientation states with a coherent lattice connection contain an elastically undeformed lattice, i.e., a prototypic phase of high symmetry [4–6], which allows not only soliton motion driven by elastic stress, but also permits unique lattice vibrations with enhanced symmetry in ways that are distinct from the constituent ferroelastic phase [7–9]. Clarifying the innate lattice dynamic properties of such ferroelastic domain walls can deepen understanding about the hidden symmetry and relevant phenomena of the walls and illuminate features of their spatially confined phononic transmission.

The primary features of Raman spectra at the domain walls have been disclosed by analyzing intensity changes, frequency shifts, and full width at half maximum (FWHM) changes of particular modes in ferroelastic or ferroelectric materials such as LiNbO₃, NdGaO₃, Gd₂(MoO₄)₃, and Pb₃(PO₄)₂ [7–14]. The frequency shifts at the domain walls in those kinds of materials were intensively described by using the concept of defects, strain, polarization reversal, and relaxation of selection rules [8–11,15,16]. Meanwhile, the direct mechanism of the intensity changes at the walls has not been sufficiently addressed [7,12–14]. Although the light-polarization dependence of Raman intensity can give reliable evidence of the point group symmetry by constructing the Raman tensor [9],

the narrow widths of ferroelastic walls have hindered direct observation of the interfacial phononic modes.

We employed tungsten trioxide WO₃, a widely studied ferroelastic material with a herringbone shaped domain structure [17–21]. The hierarchical domain texture consists of stripe ordered macrodomains (a few micrometers), which is composed of fine domains (a few tens of nanometers) [21]. The rather large width of the wall has been found in relation to the small Young's modulus and high dielectric constant of such A-site vacant perovskite WO₃ [17]. Flexoelectric polarization and flexopiezoelectric response have been observed, resulting from the existence of a large strain gradient across the macrodomain wall in the WO₃ [17].

In this paper, using a confocal Raman spectroscopy, we map the spatial distribution of the ferroelastic domain textures depending on the linear light polarization angle. Remarkably, phononic modes including the lowest Raman shift ~46 cm⁻¹ showed significantly large enhancement at the walls, while the other phonon modes undergo intensity suppression. We discuss the origin of the interfacial contribution based on the spontaneous-strain-induced modification of the Raman scattering tensor.

II. EXPERIMENT

We deposited an ultrathick WO₃ film (2–4 μm in thickness) on an orthorhombic (110)_O YAlO₃ substrate using pulsed laser deposition (see Sec. 1 of the Supplemental Material [22]). The surface topographic image revealed surface modification of the ferroelastic domain textures, as well as an atomically flat step-terrace structure. The pseudocubic lattice parameters of the WO₃ film were determined to be $a = 3.656 \text{ \AA}$, $b = 3.759 \text{ \AA}$, $c = 3.848 \text{ \AA}$, and $\beta_m = 89.18^\circ$, which correspond to the monoclinic phase (space group $P2_1/n$, Hermann-Mauguin notation) [17,21]. From here, all the

*These authors contributed equally to this work.

†yong.hyun.kim@kaist.ac.kr

‡chyang@kaist.ac.kr

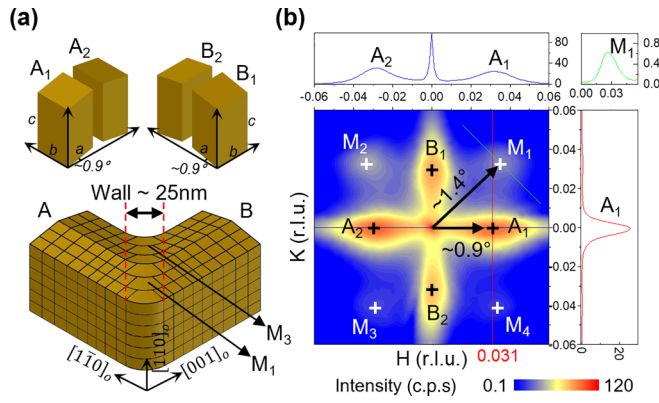


FIG. 1. (a) Schematics of the WO₃ monoclinic unit cells (A_1 , A_2 , B_1 , and B_2) along the $[001]_0$ or $[1\bar{1}0]_0$ direction of the YAIO₃ substrate. (b) X-ray HK reciprocal space map of the WO₃ (002) peak identifies the mosaic rotation angles (0.9°) of the monoclinic unit cells in the A/B domains. The M_1 , M_2 , M_3 , and M_4 peaks indicate the pseudocubic $[110]$, $[\bar{1}10]$, $[\bar{1}\bar{1}0]$, and $[1\bar{1}0]$ directions of the macrodomain walls, respectively.

symmetry notations of the space groups and the point groups are represented by Hermann-Mauguin notation for consistency. Reciprocal space maps (RSMs) for the WO₃ film on YAIO₃ substrate were measured at Pohang Accelerator Laboratory (beamline 3A). The angle-resolved polarized Raman spectra and mapping images were measured by confocal Raman spectroscopy (WITec Alpha 300 R). The excitation wavelength was 633 nm with a laser power of 17 mW. The physical unit of the spectral intensity was charge coupled device counts (CCD cts) with an integration time of 0.01 s. The laser beam was focused onto the sample surface, forming a spot diameter of ~ 429 nm through an optical lens with a numerical aperture of 0.9. We employed the Vienna Ab-initio Simulation Package (VASP) code [31], PHONOPY software [32], and the PHONOPY-spectroscopy code [33] to numerically calculate the phonon dispersion, phonon eigenvector, irreducible representation, and Raman intensity of each vibrational mode for bulk monoclinic $P2_1/n$ (space group) WO₃ (for details, see Sec. 7 of the Supplemental Material [22]).

III. RESULTS AND DISCUSSION

Ferroelastic WO₃ has four types of orientation states, denoted A_1 , A_2 , B_1 , and B_2 , which are called fine domains, shown in Fig. 1(a). The A and B domains are identical in their crystal structure but differ from each other by an azimuthal rotation of $\pm 90^\circ$ [17,21]. Since the pseudocubic lattice parameters a and b of WO₃ can either be smaller or larger than the in-plane lattice parameters of the substrate, the alternating occurrence of A and B domains effectively minimizes the misfit strain from the substrate [21]. These so-called macrodomains appear in a striped pattern along $\langle 110 \rangle$.

To characterize the structure of the ferroelastic domain walls, we carried out x-ray diffraction and examined the diffusive nature of the superlattice peaks around the WO₃ (002) pseudocubic peak. Figure 1(b) is a quasi- HK reciprocal space map obtained by multiple ω -rocking scans at different azimuthal angles. From this map, we were able to identify the

mosaic rotations of monoclinic unit cells by observing the pseudocubic (002) peaks on the H or K axes, which deviated from the center by a mosaic rotation angle ($\pm 0.9^\circ$). Four kinds of mosaic rotations, labeled A_1 , A_2 , B_1 , and B_2 , were identified. What was notable was the weak superlattice M peaks appearing along $\langle 110 \rangle$ due to the macrodomain walls. The FWHM of the M_1 peak along the transverse direction (green line) led to a wall width estimate of ~ 26.5 nm [$= \sim 3.71 \text{ \AA} / 0.014$, see Fig. 1(b)], which is consistent with the reported value (~ 20 nm) directly confirmed by scanning transmission electron microscopy [17].

Polarized Raman scattering of a WO₃ film was performed with a normal-incidence (Z) backscattering (\bar{Z}) geometry, in which the direction of the incident and scattered lights is parallel or antiparallel to the Z direction, which is opposite to the c -axis direction of the WO₃ film. The X and Y directions in the sample stage were set to be parallel to the in-plane orthorhombic $[1\bar{1}0]_0$ and $[001]_0$ directions of the substrate, respectively. In the following, θ_p stands for the angle of light polarization with respect to the X direction when the angles of the polarizer and analyzer are equal, i.e., in the parallel-polarization geometry shown in Fig. 2(c). The 48 Raman active modes of the monoclinic $2/m$ (point group) can be characterized using the possible irreducible representations, $\Gamma = 24A_g + 24B_g$ [34–36]. According to the polarization selection rule [37], all the peaks observed in $\theta_p = 0^\circ$ and 90° were assigned to the A_g normal modes rather than the B_g normal modes, because the peaks were negligibly measured in the perpendicular-polarization geometry (Supplemental Material Fig. S2 [22]).

To identify the correlation between the phononic Raman contrast and the domain texture presumed from the surface topography, we performed polarized Raman mapping at a wave number of 709 cm^{-1} with $\theta_p = 90^\circ$ [Fig. 2(a)]. Diagonal stripe domains were observed with a typical width of $\sim 3 \mu\text{m}$ for a single domain. The bright and dark regions had distinct spectra depending on whether the linear light polarization was parallel or perpendicular to the monoclinic ca plane [Fig. 2(b)]. By comparing the spectra of the A and B domains as the light polarization changed (Supplemental Material Fig. S2 [22]), we confirmed that the difference between the bright and dark regions originates from a 90° rotation of the polarization configuration, indicating that the macrodomains are responsible for the Raman domain pattern.

We systematically acquired Raman images at the wave number of 46 cm^{-1} by varying the parallel-polarization configurations, such as $\theta_p = 0^\circ, 45^\circ, 90^\circ$, and 135° over an identical area [Fig. 3(a)], and then extracted representative line profiles [Fig. 3(b)]. Similar to the earlier mode, the bright and dark contrast in the maps of $\theta_p = 0^\circ$ and 90° could be mainly attributed to the A/B domains, but the contrast was reversed. Interestingly, we noted the bright-contrast domain had two shoulders with positions close to the walls. These shoulders indicate Raman enhancement occurs at the walls, which is superimposed on the gradual change in the corresponding Raman signal across the boundary of A/B domains (Supplemental Material Fig. S5 [22]). Additionally, the mapping images at $\theta_p = 45^\circ$ and 135° showed clearly intense peaks only at the boundaries between the A and B domains, implying the intensity enhancement at the domain wall. Based

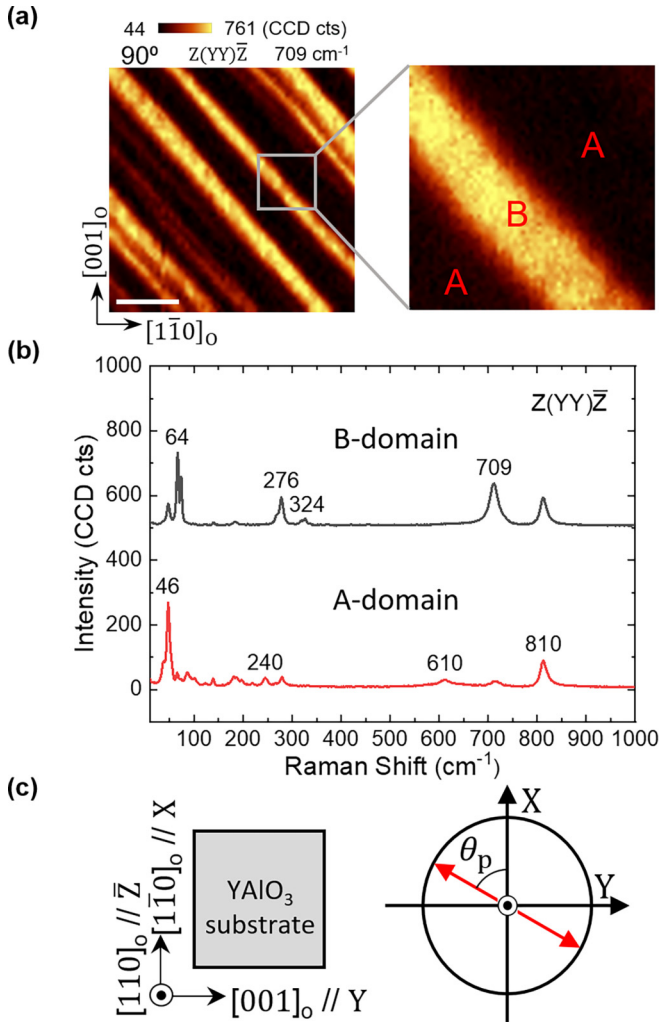


FIG. 2. (a) Polarized Raman mapping of the stripe *A* and *B* domains (709 cm⁻¹) with a polarization configuration of $Z(Y\bar{Y})\bar{Z}$ expressed by the Porto notation. Scale bar indicates 3 μm . (b) Raman spectra obtained from bright *B* (black solid line) and dark *A* (red solid line) macrodomain regions. (c) The *X* and *Y* light polarization directions are parallel to the $[1\bar{1}0]_0$ and $[001]_0$ directions of the YAlO_3 substrate, respectively.

on the simulation results for Raman intensity depending on the geometrical distribution [Fig. 3(c)], the intrinsic vibrational signal of the wall has approximately three times larger intensity than that of the *B* domain, assuming that the domain wall width is 25 nm and the laser spot size is 429 nm (Supplemental Material Fig. S5 [22]). A similar interfacial enhancement was observed not only at the wave number of 46 cm⁻¹ but also at 240, 610, and 810 cm⁻¹ (Supplemental Material Fig. S8 [22]).

Since the macrodomain walls have a strong strain gradient of as much as 10⁶ m⁻¹, the enhancement in Raman signals could be due to either a flexophenomenon, i.e., an effect proportional to the strain gradient, or to a piezophenomenon attributed to an interfacial strain state distinct from the ferroelastic phase. To clarify the origin of the Raman enhancement, we experimentally characterized the Raman tensor (\vec{R} , 3×3 matrix) components of the domain and wall regions using angle-resolved polarized Raman scattering (Fig. 4). The Ra-

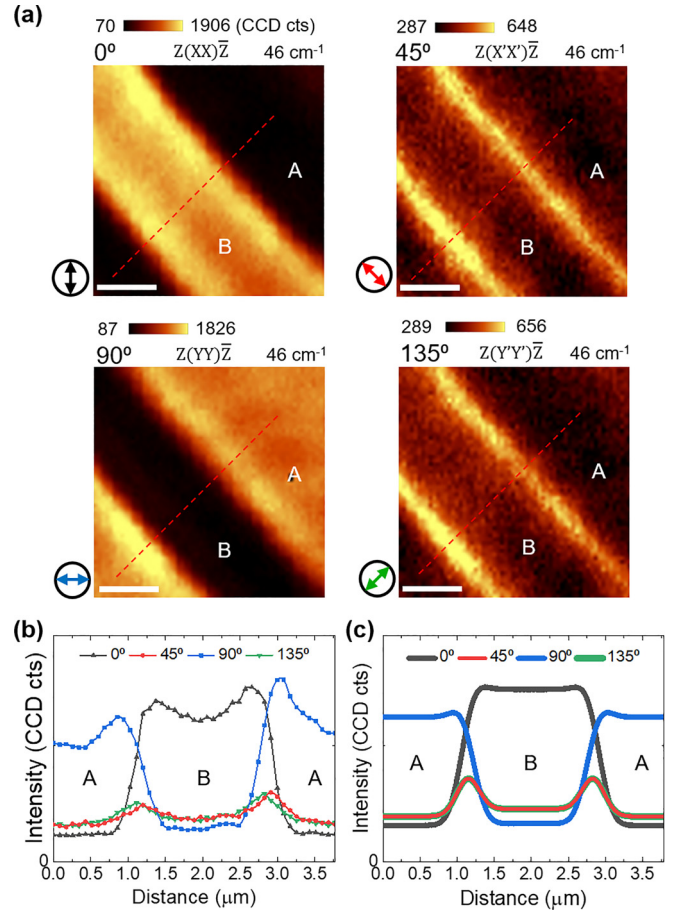


FIG. 3. (a) Polarized Raman mapping of domains and walls (46 cm⁻¹) with 0°, 45°, 90°, and 135° polarization angles at the same region. Scale bars indicate 1 μm . (b) The line profiles were obtained for an identical region (red dashed line) of each Raman image. (c) The line profiles were theoretically simulated considering the geometrical distribution of the domain and wall structure, and the light convolution effect.

man tensor of the A_g normal mode of the WO_3 monoclinic structure (point group $2/m$) is represented as (for specifics, see Sec. 3 of the Supplemental Material [22])

$$\vec{R}_{A_g} = \begin{pmatrix} \alpha & 0 & \delta \\ 0 & \beta & 0 \\ \delta & 0 & \gamma \end{pmatrix}. \quad (1)$$

For the parallel scattering configuration, the Raman intensity (I) can be obtained as [38,39]

$$I_{A_g}^{\parallel} \propto |\alpha|^2 (\cos \theta_p)^4 + |\beta|^2 (\sin \theta_p)^4 + \frac{1}{2} |\alpha| |\beta| (\sin 2\theta_p)^2 \cos \varphi_{\alpha\beta}, \quad (2)$$

where $\varphi_{\alpha\beta} = \varphi_{\alpha} - \varphi_{\beta}$ is the phase difference between the α and β components. Experimental Raman intensities for the *A/B* domains and wall were acquired as a function of θ_p in the range 0–180° with parallel-polarization configuration. The intensity curves of the *A* and *B* domains were twofold lobe shapes that well fit the expected lines of Eq. (2), as shown in Figs. 4(a) and 4(b), respectively. The values of the anisotropy

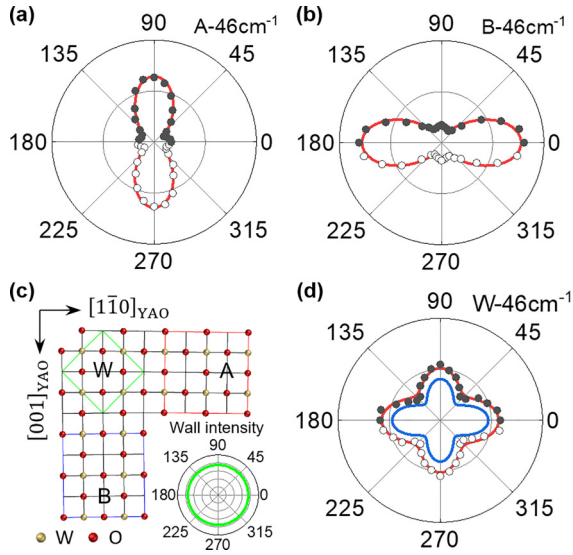


FIG. 4. Angular dependence ($0\text{--}180^\circ$) of the Raman intensity (46 cm^{-1}) on the parallel-polarization configuration. The experimental data (black solid circles) and the point symmetric position (black open circles) were fitted (red solid line) using the $\overleftrightarrow{R}_{A_g}$ Raman tensor for the A (a) and B (b) domains. (c) Schematics of the unit cells for A (red) and B (blue) domains and wall (green). Raman intensity curve of the $\overleftrightarrow{R}_{A_{1g}}$ Raman tensor of the pristine phase in the domain wall (inset). (d) The experimental data (black solid circle) of the domain wall were fitted (red solid line) using the simulation of intensity for the A/B domains and the wall. The blue solid line indicates the average value of the A/B domains. All radial scales are the same as the 200 CCD cts.

ratio $|\beta|/|\alpha|$ were 1.98 ± 0.03 (A domain) and 0.46 ± 0.01 (B domain).

The polar plot of the wall area cannot be described as a linear combination of only the A and B domain plots as shown in Fig. 4(d). In particular, the $\langle 110 \rangle$ directions ($\theta_p = 45^\circ$ and 135°) have a considerable Raman intensity, a feature which is distinct from the domain regions [Fig. 3(a)]. The wall region should satisfy the strain compatibility relation which results in the same extent of length modification from the prototypic phase in all directions at the boundaries between the two adjacent domains due to spontaneous strains [4]. Referring to the gradual and coherent lattice connection of the WO_3 unit cells, even at the wall, it is natural that the closer the unit cell of the ferroelastic material is to the wall, the closer it is to that of its prototype since the two different spontaneous strains are compensated with each other. Therefore, the spontaneous strain of the twin wall can be mathematically derived by the average value of the spontaneous strains of the two adjacent domains as

$$\frac{X_S(S_1) + X_S(S_2)}{2} = X_S(W_{S_1/S_2}), \quad (3)$$

where X_S is the spontaneous strain tensor, and S_1 , S_2 and W_{S_1/S_2} stand for particular orientation states of the ferroelastic crystal, and the domain boundary between the two orientation states, respectively. The spontaneous strains for A_1 , A_2 , B_1 , and B_2 domains are given by (for specifics, see Sec. 6 of the

Supplemental Material [22])

$$X_S(A_1) = \begin{pmatrix} -\lambda & 0 & \mu \\ 0 & \lambda & 0 \\ \mu & 0 & 0 \end{pmatrix}, \quad X_S(A_2) = \begin{pmatrix} -\lambda & 0 & -\mu \\ 0 & \lambda & 0 \\ -\mu & 0 & 0 \end{pmatrix},$$

$$X_S(B_1) = \begin{pmatrix} \lambda & 0 & 0 \\ 0 & -\lambda & \mu \\ 0 & \mu & 0 \end{pmatrix}, \quad X_S(B_2) = \begin{pmatrix} \lambda & 0 & 0 \\ 0 & -\lambda & -\mu \\ 0 & -\mu & 0 \end{pmatrix}, \quad (4)$$

where $\lambda = |\frac{a-l}{l}| \approx 0.013$ and $\mu = |\frac{\tan 0.8^\circ}{2}| \approx 0.007$ are the normal strain and the shear strain, respectively. Therefore, the spontaneous strains for the A_1/B_1 and A_2/B_2 macrodomain walls can be obtained using Eq. (3) as

$$X_S(W_{A_1/B_1}) = \begin{pmatrix} 0 & 0 & \mu/2 \\ 0 & 0 & \mu/2 \\ \mu/2 & \mu/2 & 0 \end{pmatrix},$$

$$X_S(W_{A_2/B_2}) = \begin{pmatrix} 0 & 0 & -\mu/2 \\ 0 & 0 & -\mu/2 \\ -\mu/2 & -\mu/2 & 0 \end{pmatrix}. \quad (5)$$

On the basis of these spontaneous strains, the lattice constants of the macrodomain walls are simply calculated as $a_t = b_t = 5.243\text{ \AA}$, $c_t = 3.848\text{ \AA}$, $\alpha_t = \gamma_t = 90^\circ$, $\beta_t = 89.59^\circ$ (not pseudocubic unit cell), which correspond to a monoclinic m (point group) considerably close to the prototypic phase of a tetragonal $4/mmm$ (point group), i.e., a quasitetragonal structure as shown in Fig. 4(c) [40]. All of these W -type macrodomain walls correspond to the diffusive peaks of $M_1(W_{A_1/B_1})$, $M_2(W_{B_1/A_2})$, $M_3(W_{A_2/B_2})$, and $M_4(W_{B_2/A_1})$ in the RSM results [Fig. 1(b)]. According to previous research, a qualitative model of the ferroelastic twin wall, i.e., layer group, which is derived from the parent clamping approximation, coincides with our results [5]. In the light of the lattice constant, our model of the strain compatibility proposes a more specific information of the crystal symmetry of the domain wall.

In the case of the macrodomain wall, the possible Raman tensor of A_{1g} normal mode in the quasitetragonal structure ($4/mmm$ of point group) can be represented as

$$\overleftrightarrow{R}_{A_{1g}} = \begin{pmatrix} \alpha_{\text{tet}} & 0 & 0 \\ 0 & \alpha_{\text{tet}} & 0 \\ 0 & 0 & \gamma_{\text{tet}} \end{pmatrix}. \quad (6)$$

The involvement of the tetragonal B_{1g} mode was ruled out by symmetry consideration. For the parallel scattering configuration, the Raman intensity of the wall can be calculated as $I \propto |\alpha_{\text{tet}}|^2$ independent of θ_p [inset of Fig. 4(c)] [38]. The resolution limit of the laser beam ($\sim 429\text{ nm}$) involves not only the wall ($\sim 25\text{ nm}$) intensity but also the A/B domain intensities, thereby the areal fractions of the A/B domains and the wall are 46.3%, 46.3%, and 7.4%, respectively (Supplemental Material Fig. S9(b) [22]). The Raman intensity summation of the A/B domains (46.3% of each domain) and the wall (7.4% of $I \propto |\alpha_{\text{tet}}|^2$) with a fitting parameter of I shows a good agreement with the experimental polar-plot data, as shown in Fig. 4(d). This also indicates that the intrinsic intensity of the wall is approximately 2.32 times larger than the maximum intensity of the B domain. The value agrees with the factor of 3, which was previously inferred from the simulation of the spatial distribution of Raman intensity [Fig. 3(c)]. Consequently, the

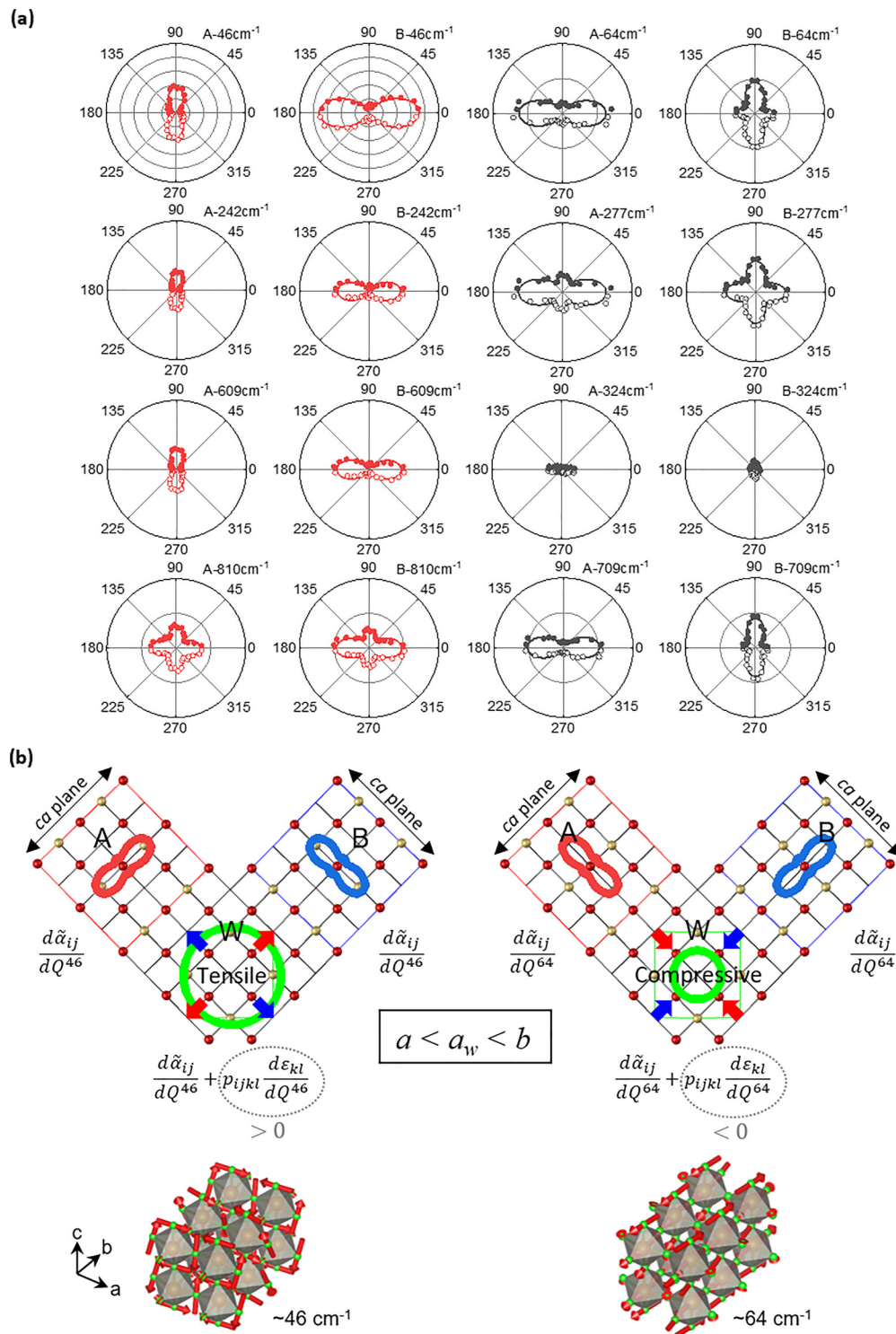


FIG. 5. (a) Angular dependence (0–180°) of the Raman intensity on the parallel polarization configuration with 532-nm laser beam in the $\sim 2\text{-}\mu\text{m}$ -thick sample. The experimental data (solid circles) and the point symmetric position (open circles) were fitted (solid line) using the $\overleftrightarrow{R}_{Ag}$ Raman tensor for each normal mode. The peaks which become larger in intensity when the light linear polarization is parallel to the monoclinic ca plane are colored red, while the peaks which become larger in intensity when the light linear polarization is perpendicular to the monoclinic ca plane are colored black. All radial scales are same as 2500 CCD cts. (b) Relation between the vibrational normal coordinate and the strain at the macrodomain wall. Intensity enhancement (46 cm^{-1}) or suppression (64 cm^{-1}) occurs depending on tensile or compressive strains along the principal axis (parallel to the lobe orientation), respectively. The red (blue) arrows indicate the directions of elastic stress for the vibrational normal modes in the A domain (B domain). Note the a -lattice parameter is smaller than b -lattice parameter, and the lattice parameters of the tetragonal walls fall in between. The inset of schematics indicates the corresponding vibrational normal coordinate by DFT calculation. W (O) atoms and their motions are represented by the orange (green) circles and red arrows, respectively.

phonon characteristics of the macrodomain wall in the WO_3 film can be explained by the $\overleftrightarrow{R}_{A_{1g}}$ Raman tensor of the prototypic quasitragonal structure. This symmetric structure of the domain wall is also consistent with the previous DFT (density functional theory) study which calculated the ferroelectric Ising type domain wall structure [16]. Simultaneously observed is no noticeable flexoelectrical modification that is expected to be anisotropic in the polar plot.

Figure 5(a) shows angle-dependent Raman intensities acquired with azimuthally rotating linear light polarization in A/B domains. In the modes of 46, 242, 609, and 810 cm^{-1} , colored red, the intensity becomes maximum as the light polarization is parallel to the monoclinic ca plane. This kind of mode results in enhancement of Raman intensity at the wall. The modes of 83, 140, 180 cm^{-1} , etc. [not shown in Fig. 5(a)] show similar behavior. On the other hand, in the modes of 64, 276, 324, and 709 cm^{-1} , colored black, the intensity becomes maximum as the light polarization is perpendicular to the monoclinic ca plane. These modes reveal suppression of Raman intensity at the wall. Whether the Raman peak is enhanced or suppressed at the wall is related to the lobe orientation of the twofold angle-dependent polar plot.

The strong Raman intensity along the lobe axis suggests the corresponding Raman mode is primarily involved in a lattice vibration along the axis. The lattice parameter b is greater than a in the domain and the in-plane lattice parameter of the quasitragonal structure at the wall is in the middle. The strain change $\Delta\varepsilon (= \varepsilon_{\text{wall}} - \varepsilon_{\text{domain}})$ between the wall and the domain along the principal axis can be either tensile or compressive depending on the type of lobe orientation. Referring to the coherent lattice connection of WO_3 unit cells at the wall [17], the vibrational normal modes parallel to the monoclinic ca plane such as 46, 242, 609, and 810 cm^{-1} are affected by the tensile strain at the wall, while the vibrational normal modes perpendicular to the monoclinic ca plane such as 64, 276, 324, and 709 cm^{-1} are affected by the compressive strain at the wall, as described in Fig. 5(b). Fontana *et al.* phenomenologically described local influences of mechanical stress acting on the Raman intensity based on the elasto-optic effect [7]. Raman intensity (I) depends on the derivative of the polarizability (α) with respect to the vibrational normal coordinate (Q),

$$I \propto \left(\frac{\partial \alpha}{\partial Q} \right)^2. \quad (7)$$

The electric polarizability affected by strain change can be written as [7]

$$\alpha = \tilde{\alpha}_0 + \frac{\partial \alpha}{\partial \varepsilon} \Delta \varepsilon, \quad (8)$$

where $\tilde{\alpha}_0$ is the polarizability at uniform strain and ε is the local strain. Thus, the Raman intensity can be related to the

following expression [7]:

$$\frac{d\alpha_{ij}}{dQ^n} = \frac{d\tilde{\alpha}_{ij}}{dQ^n} + \frac{\partial \alpha_{ij}}{\partial \varepsilon_{kl}} \frac{d\varepsilon_{kl}}{dQ^n} = \frac{d\tilde{\alpha}_{ij}}{dQ^n} + p_{ijkl} \frac{d\varepsilon_{kl}}{dQ^n}, \quad (9)$$

where Q^n is the vibrational normal coordinate of the n th phonon mode and p_{ijkl} is the elasto-optic coefficient. This implies that strain at the wall can modify Raman intensity through the elasto-optic term

$$p_{ijkl} \frac{d\varepsilon_{kl}}{dQ^n}. \quad (10)$$

This strain induced term under a tensile strain has the plus sign, which induces the enhancement of Raman intensity. On the other hand, under a compressive strain, the term has the minus sign, which induces the suppression of Raman intensity. Accordingly, whether the intensity increases or decreases at the wall depends on whether the vibrational normal mode undergoes tensile or compressive strains. According to the DFT calculations, the directions of vibrational normal coordinates in the 46- and 64-cm^{-1} modes were in good agreement with the Raman intensity variations, which are low-energy rotational vibration modes.

IV. CONCLUSION

In summary, the phononic modes of ferroelastic macrodomain walls in WO_3 films have been characterized by angle-resolved polarized Raman scattering. The intensity enhancement of the wall was carefully examined at a Raman shift of 46 cm^{-1} , indicating the wall intensity per unit area is approximately three times higher than the maximum intensity observed in the domains. The light-polarization dependence at the wall was isotropic and was described by the $\overleftrightarrow{R}_{A_{1g}}$ Raman tensor of a quasitragonal structure, in contrast to the twofold lobe-shaped dependence in the domain. Furthermore, we observed that other Raman modes are also enhanced or suppressed at the wall. We found empirically that enhancement or suppression is directly related to the polar-plot symmetry (i.e., lobe orientation) of the corresponding mode in the domains and discussed the origin based on the elasto-optic effect. Our observations provide a good example of prototypical domain walls of which the properties are forced by domain properties.

ACKNOWLEDGMENTS

This work was supported by the National Research Foundation (NRF) of Korea Grants funded by the Korean Government via the Creative Research Center for Lattice Defectronics (Grant No. NRF-2017R1A3B1023686) and the Center for Quantum Coherence in Condensed Matter (Grant No. 2016R1A5A1008184). It was also supported by Samsung Electronics Co., Ltd. (Grant No. IO201211-08093-01).

[1] G. Catalan, J. Seidel, R. Ramesh, and J. F. Scott, *Rev. Mod. Phys.* **84**, 119 (2012).
 [2] E. K. H. Salje, *Annu. Rev. Mater. Res.* **42**, 265 (2012).

[3] J. Seidel, L. W. Martin, Q. Zhan, Y.-H. Chu, A. Rother, M. E. Hawkrige, P. Maksymovych, P. Yu, M. Gajek, N. Balke, S. V. Kalinin, S. Gemming, F. Wang, G. Catalan, J. F. Scott,

- N. A. Spaldin, J. Orenstein, and R. Ramesh, *Nat. Mater.* **8**, 229 (2009).
- [4] J. Sapriel, *Phys. Rev. B* **12**, 5128 (1975).
- [5] V. Janovec and J. Privratska, in *International Tables for Crystallography* (Wiley, New York, 2013), Vol. D, Chap. 3.4, pp. 484–543.
- [6] P. Toledano, M. Guennou, and J. Kreisel, *Phys. Rev. B* **89**, 134104 (2014).
- [7] M. D. Fontana, R. Hammoum, P. Bourson, S. Margueron, and V. Ya. Shur, *Ferroelectrics* **373**, 26 (2008).
- [8] P. S. Zelenovskiy, V. Ya. Shur, P. Bourson, M. D. Fontana, D. K. Kuznetsov, and E. A. Mingaliev, *Ferroelectrics* **398**, 34 (2010).
- [9] G. F. Nataf and M. Guennou, *J. Phys.: Condens. Matter* **32**, 183001 (2020).
- [10] G. F. Nataf, M. Guennou, A. Haubmann, N. Barrett, and J. Kreisel, *Phys. Status Solidi RRL* **10**, 222 (2016).
- [11] G. F. Nataf, N. Barrett, J. Kreisel, and M. Guennou, *J. Phys.: Condens. Matter* **30**, 035902 (2018).
- [12] I. W. Shepherd and J. R. Barkley, *Solid State Commun.* **10**, 123 (1972).
- [13] B. Mihailova, U. Bismayer, A. Engelhardt, and B. Guttler, *J. Phys.: Condens. Matter* **13**, 9383 (2001).
- [14] U. Bismayer, B. Mihailova, and R. Angel, *J. Phys.: Condens. Matter* **29**, 213001 (2017).
- [15] G. Stone, B. Knorr, V. Gopalan, and V. Dierolf, *Phys. Rev. B* **84**, 134303 (2011).
- [16] M. Rusing, S. Neufeld, J. Brockmeier, C. Eigner, P. Mackwitz, K. Spychala, C. Silberhorn, W. G. Schmidt, G. Berth, A. Zrenner, and S. Sanna, *Phys. Rev. Mater.* **2**, 103801 (2018).
- [17] S. Yun, K. Song, K. Chu, S.-Y. Hwang, G.-Y. Kim, J. Seo, C.-S. Woo, S.-Y. Choi, and C.-H. Yang, *Nat. Commun.* **11**, 4898 (2020).
- [18] S. Tanisaki, *J. Phys. Soc. Jpn* **15**, 573 (1960).
- [19] K. R. Locherer, J. Chrosch, and E. K. H. Salje, *Phase Transit.* **67**, 51 (1998).
- [20] A. Garg, *Growth and Characterization of Epitaxial Oxide Thin Films* (Cambridge University Press, Cambridge, UK, 2001).
- [21] S. Yun, C.-S. Woo, G.-Y. Kim, P. Sharma, J. H. Lee, K. Chu, J. H. Song, S.-Y. Chung, J. Seidel, S.-Y. Choi, and C.-H. Yang, *Appl. Phys. Lett.* **107**, 252904 (2015).
- [22] See Supplemental Material at <http://link.aps.org/supplemental/10.1103/PhysRevB.108.014103> for the materials synthesis, assignment of vibration normal mode, simulations of the angle dependence and line profile of Raman spectra, polarized Raman mapping for additional modes, strain compatibility of spontaneous strains, and first principles density functional calculations for phonon and Raman intensity, which includes Refs. [23–30].
- [23] W. Zheng, J. Yan, F. Li, and F. Huang, *Photon. Res.* **6**, 709 (2018).
- [24] K. Aizu, *J. Phys. Soc. Jpn.* **28**, 706 (1970).
- [25] P. E. Blöchl, *Phys. Rev. B* **50**, 17953 (1994).
- [26] R. Armiento and A. E. Mattsson, *Phys. Rev. B* **72**, 085108 (2005).
- [27] P. P. González-Borrero, F. Sato, A. N. Medina, M. L. Baesso, A. C. Bento, G. Baldissera, C. Persson, G. A. Niklasson, C. G. Granqvist, and A. Ferreira da Silva, *Appl. Phys. Lett.* **96**, 061909 (2010).
- [28] D. B. Migas, V. L. Shaposhnikov, V. N. Rodin, and V. E. Borisenko, *J. Appl. Phys.* **108**, 093713 (2010).
- [29] H. Zheng, J. Z. Ou, M. S. Strano, R. B. Kaner, A. Mitchell, and K. Kalantar-zadeh, *Adv. Funct. Mater.* **21**, 2175 (2011).
- [30] C. J. Howard, V. Luca, and K. S. Knight, *J. Phys.: Condens. Matter* **14**, 377 (2002).
- [31] G. Kresse and J. Hafner, *Phys. Rev. B* **47**, 558 (1993).
- [32] A. Togo and I. Tanaka, *Scr. Mater.* **108**, 1 (2015).
- [33] J. M. Skelton, L. A. Burton, A. J. Jackson, F. Oba, S. C. Parker, and A. Walsh, *Phys. Chem. Chem. Phys.* **19**, 12452 (2017).
- [34] G. N. Kustova, Y. A. Chesalov, L. M. Plyasova, I. Y. Molina, and A. I. Nizovskii, *Vib. Spectrosc.* **55**, 235 (2011).
- [35] S. Bhagavantam and T. Venkatarayudu, *Theory of Groups and its Application to Physical Problems* (Academic Press, New York, 1969).
- [36] E. Salje, *Acta Cryst.* **A31**, 360 (1975).
- [37] R. Loudon, *Adv. Phys.* **13**, 423 (1964).
- [38] T. Strach, J. Brunen, B. Lederle, J. Zegenhagen, and M. Cardona, *Phys. Rev. B* **57**, 1292 (1998).
- [39] C. Kranert, C. Sturm, R. Schmidt-Grund, and M. Grundmann, *Phys. Rev. Lett.* **116**, 127401 (2016).
- [40] W. L. Kehl, R. G. Hay, and D. Wahl, *J. Appl. Phys.* **23**, 212 (1952).